Refractory solid condensation detected in an embedded protoplanetary disk

McClure, M.K.; van't Hoff, M.; Francis, L.; Bergin, E.; Rocha, W.R.M.; Sturm, J.A.; ... ; Dartois, E.

Citation

McClure, M. K., Van't Hoff, M., Francis, L., Bergin, E., Rocha, W. R. M., Sturm, J. A., ... Dartois, E. (2025). Refractory solid condensation detected in an embedded protoplanetary disk. *Nature*, *643*(8072), 649-653. doi:10.1038/s41586-025-09163-z

Refractory solid condensation detected in an embedded protoplanetary disk

https://doi.org/10.1038/s41586-025-09163-z

Received: 23 July 2024

Accepted: 15 May 2025

M. K. McClure[1]✉, Merel van't Hoff[2,3], Logan Francis[1], Edwin Bergin[2], Will R. M. Rocha[1,4], J. A. Sturm[1], Daniel Harsono[5], Ewine F. van Dishoeck[1], John H. Black[6], J. A. Noble[7], D. Qasim[8] & E. Dartois[9]

Terrestrial planets and small bodies in our Solar System are theorized to have assembled from interstellar solids mixed with rocky solids that precipitated from a hot, cooling gas[1,2]. The first high-temperature minerals to recondense from this gaseous reservoir start the clock on planet formation[3,4]. However, the production mechanism of this initial hot gas and its importance to planet formation in other systems are unclear. Here we report the astronomical detection of this $t = 0$ moment, capturing the building blocks of a new planetary system beginning its assembly. The young protostar HOPS-315 is observed at infrared and millimetre wavelengths with the James Webb Space Telescope (JWST) and the Atacama Large Millimeter Array (ALMA), revealing a reservoir of warm silicon monoxide gas and crystalline silicate minerals low in the atmosphere of a disk within 2.2 AU of the star, physically isolated from the millimetre SiO jet. Comparison with condensation models with rapid grain growth and disk structure models suggests the formation of refractory solids analogous to those in our Solar System. Our results indicate that the environment in the inner disk region is influenced by sublimation of interstellar solids and subsequent refractory solid recondensation from this gas reservoir on timescales comparable with refractory condensation in our own Solar System.

The Class I protostar HOPS-315, located in the Orion B molecular cloud at a distance of 420 pc (refs. 5–7), is an ideal target for studying the formation of the first refractory solids in other star systems. As shown in Fig. 1, it has a clear, 40° sightline through its embedding, dusty envelope to a gaseous disk accreting onto the central protostar[5,8–10]. The energy released by such accretion can heat the disk midplane to the point at which rocky grains vaporize near approximately 1,300 K (refs. 11,12), potentially resetting the interstellar dust composition to molecular and atomic gas from which only the most refractory solids can recondense[13,14].

Our Cycle 1 General Observer programme with JWST (programme 1854, principal investigator (PI) M. K. McClure) observed HOPS-315 using the integral field spectroscopy (IFU) modes of the near-infrared spectrograph (NIRSpec) and mid-infrared instrument (MIRI) with high signal-to-noise-ratio (SNR ≈ 540 at 8 μm; Methods). The high spectral resolution of these instruments reveals a rich spectrum dominated by strong absorption features of icy and rocky solids and copious gas-phase species (Fig. 2). Unusually, we detect both the SiO vibrational fundamental gas band and crystalline SiO-rich solids (silicates) in absorption. The strength of the latter is unusual for protostars[15], although similarly prominent features towards another protostar[16] were attributed to crystalline grains entrained in an outflow.

Although HOPS-315 indeed shows a prominent H_2 jet and disk wind[17,18], they probably do not carry the observed crystalline silicates. First, HOPS-315's jet is not detected in extended Fe^+ emission, a common infrared tracer[19–23], even at knots in which entrained dust grains should sputter, suggesting that the jet contains little dust. Second, HOPS-315's H_2 must emit from a hot foreground layer, whereas its crystalline dust must absorb in a cooler layer above a hot background layer. This absorbing layer is sandwiched below the hot H_2 emitting layer, as the 9.66 μm H_2 0-0 S(3) line, in the bottom of the silicate absorption complex, has a visibly higher peak-to-continuum ratio than the H_2 0-0 S(2) line outside the silicate band, implying that the silicates do not lead to extinction of the S(3) emission. Such vertically layered temperature 'inversion' patterns are predicted for disks around highly accreting stars. High-pressure, radially extended 'thermostat' regions develop at their midplanes, maintaining equilibrium between silicate vaporization and recondensation at $T_{\mathrm{sil}} \approx 1{,}300$ K (refs. 11–13), resulting in local SiO gas and crystalline silicate production, respectively[24]. This previously undetected thermostat region has been proposed as a point of origin for refractory solids in the Solar System[13,14].

We test whether the observed crystalline silicates and SiO gas are consistent with production under such physical conditions. First, we fit laboratory mineral data to the solid-state absorption features between 7.75 and 28.00 μm (Methods and Extended Data Table 1),

---

[1]Leiden Observatory, Leiden University, Leiden, The Netherlands. [2]Department of Astronomy, University of Michigan, Ann Arbor, MI, USA. [3]Department of Physics and Astronomy, Purdue University, West Lafayette, IN, USA. [4]Laboratory for Astrophysics, Leiden Observatory, Leiden University, Leiden, The Netherlands. [5]Institute of Astronomy, Department of Physics, National Tsing Hua University, Hsinchu, Taiwan. [6]Onsala Space Observatory, Department of Space, Earth and Environment, Chalmers University of Technology, Onsala, Sweden. [7]Physique des Interactions Ioniques et Moléculaires, CNRS, Aix Marseille Université, Marseille, France. [8]Southwest Research Institute, San Antonio, TX, USA. [9]Institut des Sciences Moléculaires d'Orsay, CNRS, Université Paris-Saclay, Orsay, France. ✉e-mail: mcclure@strw.leidenuniv.nl

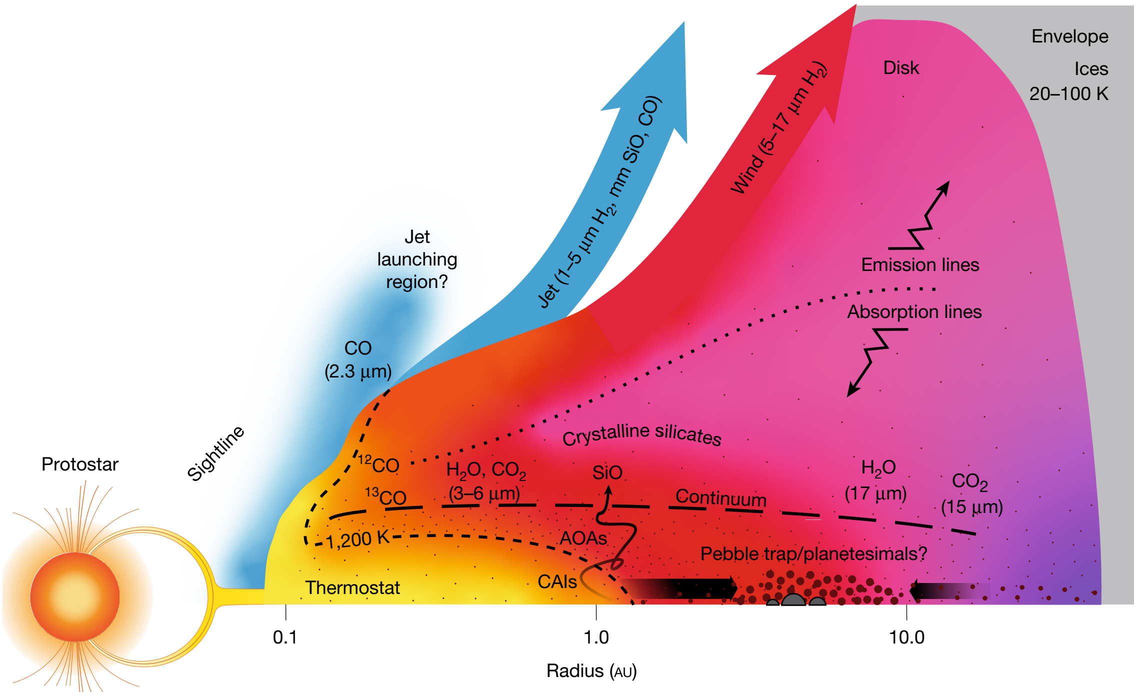

Fig. 1 | Structure of HOPS-315's inner disk. Molecules located above the temperature minimum (dotted line) are seen in emission. Molecules located between the temperature minimum and the disk photosphere (long-dashed line) are seen in absorption. Dust sublimates in the thermostat region near 1 AU (short-dashed line), releasing SiO. Turbulent transport there leads to vertical condensation of CAIs and AOAs, of which the co-spatial SiO and crystalline silicates are remnants.

identifying forsterite (Mg_2SiO_4, $N_{\rm forst} = 1.3^{+0.5}_{-0.8} \times 10^{17}$ cm^{-2}) and enstatite ($MgSiO_3$, $N_{\rm enst} = 3.7^{+0.6}_{-0.8} \times 10^{17}$ cm^{-2}) robustly (Fig. 3). Silica (SiO_2, $N_{\rm Silica} = 1.4^{+0.2}_{-0.1} \times 10^{17}$ cm^{-2}) is tentatively detected at a 3σ level (see significance discussion in Methods). The abundance ratio of $N_{\rm enst}/N_{\rm forst}$ is high at $2.8^{+5.8}_{-1.2}$. We next measure the temperature, column density and linewidth of all observed molecular gas species using slab models of line optical depths (Methods and Extended Data Table 2). The linewidth implies a rough constraint on the location of each molecule. In the absence of strong turbulence, infrared SiO absorbs near 1 AU with a column density of $N_{\rm SiO} = 4.62 \pm 0.14 \times 10^{18}$ cm^{-2} and temperature $T_{\rm SiO} = 472^{+6}_{-4}$ K, well below the silicate sublimation temperature. Cross-correlating our SiO model with the observed molecular band indicates a velocity of −10.6 ± 1.2 km s^{-1}, which is blueshifted by about 20 km s^{-1} from the millimetre system velocity of +9.68 ± 0.19 km s^{-1} (all in the velocity reference frame of the kinematic local standard of rest, $\upsilon_{\rm LSRK}$; Methods and Extended Data Fig. 1). This velocity suggests that the infrared SiO gas is flowing upward from the thermostat region into the cooler inversion layer, at which the crystalline silicates are absorbing below the H_2 emitting disk wind (that is, discussion of H_2 S(3) line above[18]), rather than in the known molecular jet[17,25].

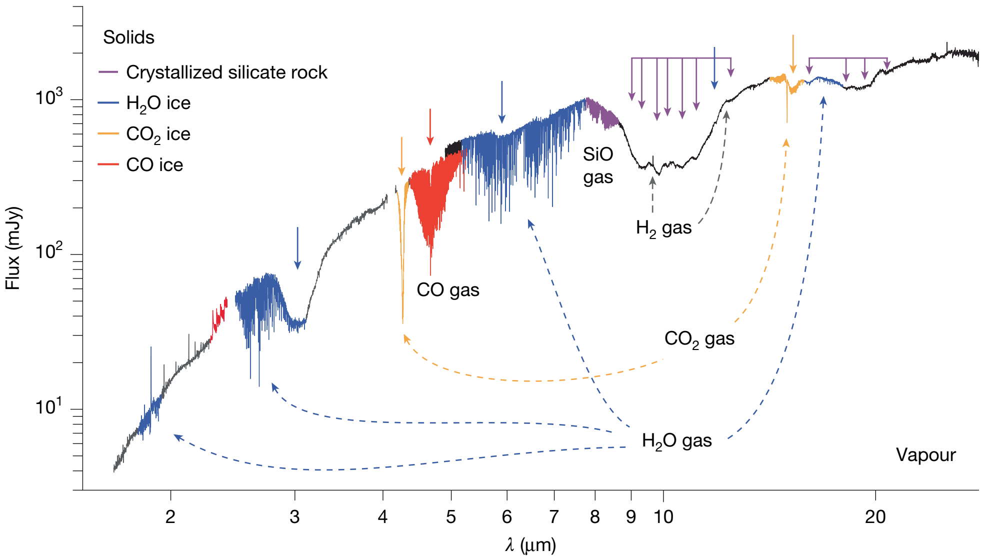

Fig. 2 | JWST spectrum of HOPS-315. Bands of ice and thermally processed silicates are seen, along with molecular gas absorption bands and (select) H_2 emission lines probing different temperatures and densities. Warm SiO gas probes vaporized rocks, whereas crystalline silicates may probe condensed SiO gas.

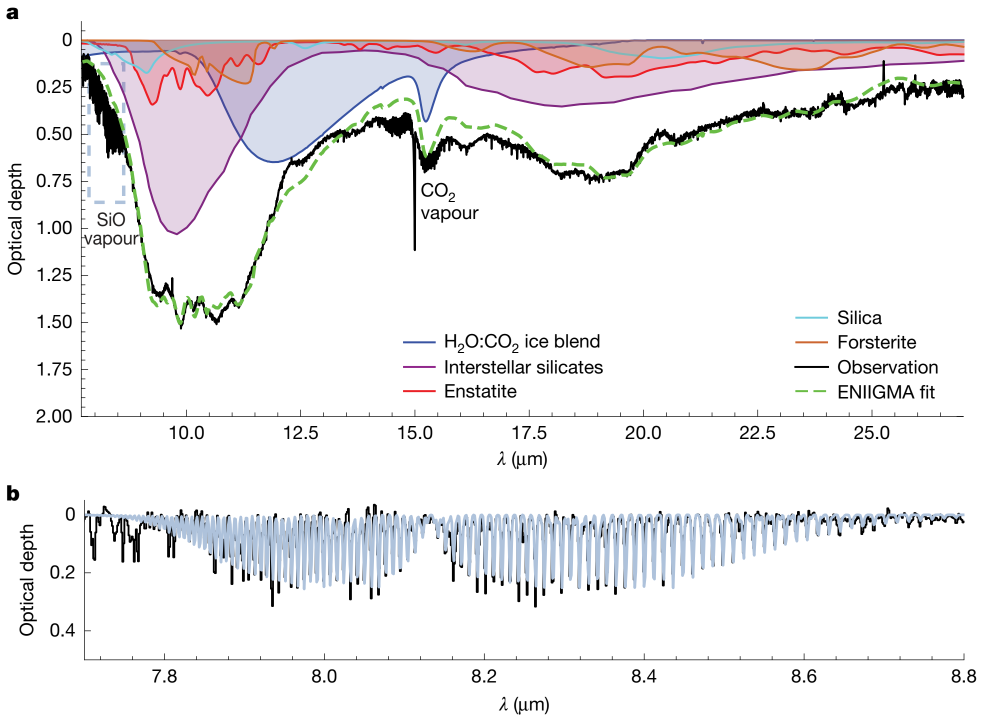

Fig. 3 | JWST crystalline silicate and SiO vapour analysis. a, Plot of the statistically significant components found by our ENIIGMA fit of laboratory mass absorption coefficients for CAI and AOA minerals. Below 18 μm, bands of 'noise' are the molecular vapour absorptions labelled in Fig. 2. The dashed box indicates the SiO gas modelled below. **b**, Slab model fit to the SiO vapour band ($\nu = 1\text{-}0\ \Sigma\text{-}\Sigma$) at 8.05 μm.

The other absorbing molecular gas species map the spatial gradients in temperature and column density of the cooler absorbing layer that is sandwiched between the hot midplane and hot, H_2 emitting disk surface (see Fig. 1, Extended Data Table 2 and Methods). The pattern of radial locations for each molecular band and the values for their temperatures broadly agree with expectations from 2D disk models for similar bands in emission[26]. The bands with moderate optical depth (for example, SiO, 17 μm H_2O) must arise just above the disk photosphere, at which the optical depth is 2/3 (ref. 11). Similar to the Sun's atmosphere, the disk photosphere must be located below the temperature minimum, to explain the absorption lines[27]. The detection of the 4.7 μm absorption band of ^{12}CO at 1,181 K implies a midplane temperature greater than 1,200 K, matching predictions of the thermostat region from disk structure models[12,14], confirming our identification.

To confirm that the SiO absorbing region and SiO jet are separate, we requested high-angular-resolution (10 AU beam size) ALMA observations of SiO, ^{12}CO and SO through a Director's Discretionary Time (DDT) proposal (PI M. van't Hoff; Methods). The millimetre SiO spectrum also shows only jet velocity components at −80 km s^{-1} and +100 km s^{-1}, and no slower component around the infrared SiO velocity of −10.6 ± 1.2 km s^{-1} (Fig. 4), confirming that the infrared SiO is not tracing the jet. Finally, the blue lobe of the millimetre SiO jet peaks 10 AU away from the star (Fig. 4), with no evidence of central emission associated with the disk. The non-detection of millimetre SiO on-source implies an infrared SiO emitting radius <2.2 AU, consistent with the 1.0–1.2 AU radius from the infrared linewidths (see Methods).

Discussion

In chemical equilibrium from solar composition gas (Mg/Si = 1.07)[2,28], refractory solids condense sequentially, beginning with calcium-rich and aluminium-rich minerals between 1,650 and 1,300 K and continuing between 1,320 and 300 K with the condensation of the minerals forsterite and enstatite, with $N_{\mathrm{enst}}/N_{\mathrm{forst}} = 0.5\text{–}0.8$ below 1,000 K (ref. 29). This sequence and gas–grain reactions exhaust the gaseous SiO, with insufficient leftovers to condense silica[29–31]. Certain meteorites contain millimetre-sized agglomerates of such minerals in the form of calcium–aluminium-rich inclusions (CAIs) and amoeboid olivine aggregates (AOAs), some of which have fine-grained (micron-sized) textures and enhanced ^{16}O isotopic signatures indicative of co-spatial condensation in the innermost solar nebula[32,33]. However, the crystalline silicates observed in protoplanetary disks[34,35] are attributed to amorphous interstellar silicates that either annealed below 1,300 K or vaporized above 1,300 K and recondensed as crystals. If HOPS-315's forsterite and enstatite are associated with AOAs formed by sublimation and recondensation, then their detection implies previous condensation of CAIs.

Several signs point to a vertical condensation origin for HOPS-315's crystalline silicates. Beyond 0.5 AU, protostellar disk models predict annealing timescales longer than the typical Class I lifetime of 0.1 Myr (ref. 14). Furthermore, the presence of 472 K SiO gas implies (partial) silicate vaporization at $T \geq 1{,}300$ K (from which SiO, Si^0, Mg^0 and Fe^0 are the main products[24]), with subsequent cooling that must be accompanied by condensation. Vertical mass flows near the water snowline are seen to advect vapour from the warm midplane to the cool temperature inversion layer, in which it recondenses, in hydrodynamical simulations of optically thick disks dominated by viscous heating[36]. An analogous mechanism at the outer edge of the thermostat region at 1 AU, combined with the increased turbulence there[37], could mix freshly sublimated SiO from the midplane into the disk atmosphere, condensing CAIs near the disk midplane and AOAs in the cooler temperature inversion layer above, explaining HOPS-315's SiO column density, blueshifted velocity and the observed crystals (Fig. 1). Whether this flow contributes to the base of the disk wind is an interesting question that could be important for understanding the outward radial transport of CAIs and AOAs by winds or viscous evolution, which are predicted to seed these solids into the comet-forming regions of disks[38–40].

The association of these crystals with AOA analogues is strengthened by HOPS-315's lack of strong Mg^0 and Fe^+ emission, despite a high SiO

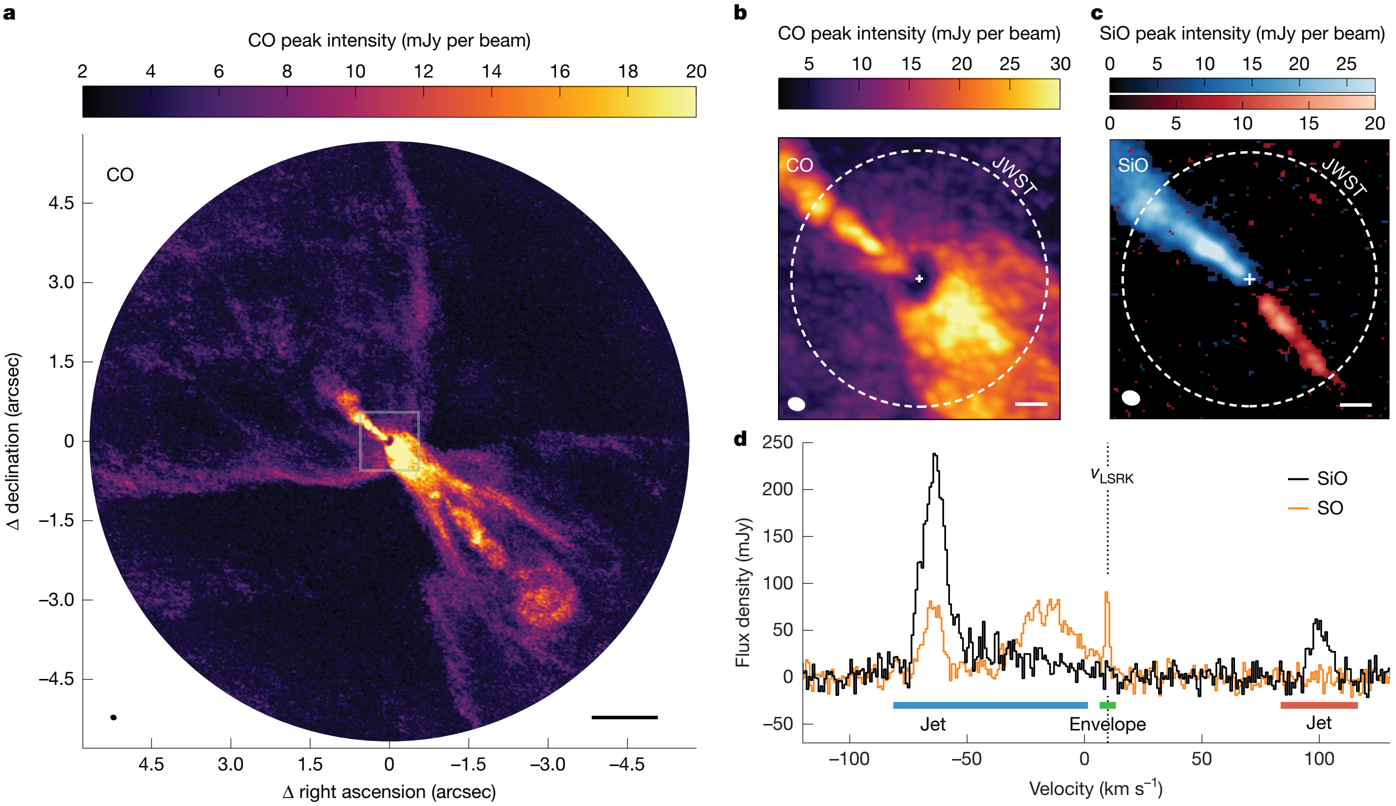

Fig. 4 | ALMA maps and spectra of HOPS-315. a, ALMA CO map showing the wide-angle outflow and molecular jet. **b**, Zoom-in on the central region of panel **a**, revealing the direct inner disk sightline, indicated by the positioning of the jet relative to the stellar location (cross) in front of the shadow caused by the optically thick dust continuum. **c**, ALMA SiO map showing the non-detection of millimetre SiO emission in the disk. **d**, SiO and SO spectra in the LSRK velocity reference frame confirm that there is no contribution to the millimetre SiO from a disk wind or gas at the source velocity. Circle is the representative JWST extraction aperture. Scale bars, 500 AU (**a**), 50 AU (**b**,**c**).

column density, which suggests that the condensing gas reservoir has a low gaseous Mg/Si ratio. This would naturally result if as little as 0.47% of the condensates became chemically isolated from the SiO reservoir, for example, by the aggregation of submicron forsterite into micron-sized agglomerates analogous to AOAs[28,31]. This decreases the efficiency of gas–grain reactions, forcing the expenditure of both Mg and SiO through enhanced enstatite condensation until the vapour Mg/Si ratio drops below unity, allowing small amounts of silica to condense from the excess SiO gas[28,29]. Condensation under solar values of Mg/Si is ruled out at a greater than 3σ level by HOPS-315's high $N_{\mathrm{enst}}/N_{\mathrm{forst}}$ of $2.8^{+5.8}_{-1.2}$, and the tentative detection of silica is consistent with this scenario. Aggregates larger than 10 µm have a grey opacity through the 10-µm feature and would not be detectable (for example, Fig. 3a of ref. 12).

Partial isolation condensation models can reproduce textures and compositions of meteoritic AOAs with 5-µm forsterite grains and silica inclusions, provided gas pressures larger than $P = 10^{-5}$ bar and vapour depletion of H and He by a factor of 10 (effectively an increase in the solids-to-gas ratio of the feedstock material[31]). Midplane pressures of the thermostat region in highly accreting disks reach $P > 10^{-5}$ bar (ref. 12), sufficient to isolate forsterite. Gravitational dust settling and inward dust motion increase the midplane solids-to-gas ratio over the interstellar value by up to a factor of 400 in the inner 1–10 AU of protostellar systems[41].

A high midplane dust/gas ratio should yield a high SiO/CO ratio in the gas accreting onto the star or launching into the jet. However, the millimetre $N_{\mathrm{SiO}}/N_{\mathrm{12CO}}$ ratio in HOPS-315's jet suggests that 98.3% of the expected silicon is missing (Methods). A dust-rich jet could explain such gas depletion, but our earlier arguments suggest that the jet and wind are dust-poor. Furthermore, the CO overtone band may probe the base of the vertically extended jet at 0.54 AU at $3{,}754^{+46}_{-44}$ K (see Extended Data Table 2). Because the SiO overtone band at 4 µm, which samples comparable temperatures, is not detected, the SiO gas may not extend towards the star. Therefore, it seems more likely that solids are sequestered outside the edge of the thermostat region.

SiO-rich solids could be preferentially retained relative to C-rich solids either through pebble trapping or planetesimal formation anywhere between the water snowline and the outer edge of the thermostat region, in which silicates vaporize[42]. The water ice snowline is the location favoured by the meteoritic record for the earliest generation of planetesimal formation, owing to signatures of hypervolatiles and oxidized iron in the known meteorite populations[43,44]. However, it is still an open question whether the Solar System's meteoritic record is complete or whether the early formation of planetesimals near the thermostat region could be possible in other protoplanetary systems (see discussion in ref. 44).

HOPS-315 shows signatures of refractory solids that probably recondensed from a high-pressure gaseous reservoir of sublimated interstellar silicates, similar to the formation conditions of AOAs and CAIs in the early Solar System. The average Class I protostellar age of 0.135 ± 0.011 Myr (Methods) is comparable with the CAI and AOA production timescale of 0.160 Myr (ref. 3); despite its unusual spectrum, HOPS-315 may represent a common protostellar evolutionary stage caught at the ideal orientation and moment of time to show these features[38]. The clear evidence for recondensation of silicates vaporized in a disk thermostat region favours the role of this region in the formation of CAIs[14], whereas the low Si/C abundance in the jet suggests that conditions are ripe for planet formation or it may already have begun. Because the Solar System's first planetesimals, iron-meteorite parent bodies, coalesced 0.1–0.3 Myr after CAI formation[45,46], HOPS-315 represents a unique opportunity to study the physical and chemical conditions during the earliest stages of planet formation, previously accessible only through the Solar System's meteoritic record.

Online content

Any methods, additional references, Nature Portfolio reporting summaries, source data, extended data, supplementary information, acknowledgements, peer review information; details of author contributions and competing interests; and statements of data and code availability are available at https://doi.org/10.1038/s41586-025-09163-z.

1. McDonough, W. F. & Sun, S. S. The composition of the Earth. *Chem. Geol.* **120**, 223–253 (1995).
2. Lodders, K. Solar System abundances and condensation temperatures of the elements. *Astrophys. J.* **591**, 1220–1247 (2003).
3. Connelly, J. N. et al. The absolute chronology and thermal processing of solids in the solar protoplanetary disk. *Science* **338**, 651–655 (2012).
4. Lichtenberg, T., Schaefer, L. K., Nakajima, M. & Fischer, R. A. Geophysical evolution during rocky planet formation. *Astron. Soc. Pac. Conf. Ser.* **534**, 907 (2023).
5. Antoniucci, S., Nisini, B., Giannini, T. & Lorenzetti, D. Accretion and ejection properties of embedded protostars: the case of HH26, HH34, and HH46 IRS. *Astron. Astrophys.* **479**, 503–514 (2008).
6. Kristensen, L. E. & Dunham, M. M. Protostellar half-life: new methodology and estimates. *Astron. Astrophys.* **618**, A158 (2018).
7. Sperling, T. et al. Probing the hidden atomic gas in Class I jets with SOFIA. *Astron. Astrophys.* **642**, A216 (2020).
8. Carr, J. S. Infrared CO emission and disks around young stars. *Astrophys. Space Sci.* **224**, 25–28 (1995).
9. Najita, J. R., Doppmann, G. W., Carr, J. S., Graham, J. R. & Eisner, J. A. High-resolution K-band spectroscopy of MWC 480 and V1331 Cyg. *Astrophys. J.* **691**, 738–748 (2009).
10. Lyo, A. R. et al. Inner warm disk of ESO Hα 279a revealed by NA I and CO overtone emission lines. *Astrophys. J.* **844**, 4 (2017).
11. D'Alessio, P., Calvet, N., Hartmann, L., Franco-Hernández, R. & Servín, H. Effects of dust growth and settling in T Tauri disks. *Astrophys. J.* **638**, 314–335 (2006).
12. McClure, M. K. et al. Curved walls: grain growth, settling, and composition patterns in T Tauri disk dust sublimation fronts. *Astrophys. J.* **775**, 114 (2013).
13. Cassen, P. Utilitarian models of the solar nebula. *Icarus* **112**, 405–429 (1994).
14. Woitke, P., Drążkowska, J., Lammer, H., Kadam, K. & Marig, P. CAI formation in the early Solar System. *Astron. Astrophys.* **687**, A65 (2024).
15. Do-Duy, T. et al. Crystalline silicate absorption at 11.1 μm: ubiquitous and abundant in embedded YSOs and the interstellar medium. *Mon. Not. R. Astron. Soc.* **493**, 4463–4517 (2020).
16. Poteet, C. A. et al. A Spitzer infrared spectrograph detection of crystalline silicates in a protostellar envelope. *Astrophys. J. Lett.* **733**, L32 (2011).
17. Davis, C. J., Stern, L., Ray, T. P. & Chrysostomou, A. Near-infrared Fabry-Perot imaging of Herbig-Haro energy sources: collimated, small-scale H_2 jets and wide-angled winds. *Astron. Astrophys.* **382**, 1021–1031 (2002).
18. Vleugels, C., McClure, M., Sturm, A. & Vlasblom, M. The H_2 jet and disk wind of the Class I protostar HOPS 315. *Astron. Astrophys.* **695**, A145 (2025).
19. Davis, C. J. et al. VLT integral field spectroscopy of embedded protostars: using near-infrared emission lines as tracers of accretion and outflow. *Astron. Astrophys.* **528**, A3 (2011).
20. Harsono, D. et al. JWST peers into the Class I protostar TMC1A: atomic jet and spatially resolved dissociative shock region. *Astrophys. J. Lett.* **951**, L32 (2023).
21. Tychoniec, Ł. et al. JWST Observations of Young protoStars (JOYS). Linked accretion and ejection in a Class I protobinary system. *Astron. Astrophys.* **687**, A36 (2024).
22. Arulanantham, N. et al. JWST MIRI MRS images of disk winds, water, and CO in an edge-on protoplanetary disk. *Astrophys. J. Lett.* **965**, L13 (2024).
23. Pascucci, I. et al. The nested morphology of disk winds from young stars revealed by JWST/NIRSpec observations. *Nat. Astron.* **9**, 81–89 (2025).
24. Gail, H. P. & Sedlmayr, E. Mineral formation in stellar winds. I. Condensation sequence of silicate and iron grains in stationary oxygen rich outflows. *Astron. Astrophys.* **347**, 594–616 (1999).
25. Dutta, S. et al. ALMA Survey of Orion Planck Galactic Cold Clumps (ALMASOP): detection of a dense SiO jet in the evolved protostellar phase. *Astrophys. J.* **925**, 11 (2022).
26. Woitke, P. et al. 2D disc modelling of the JWST line spectrum of EX Lupi. *Astron. Astrophys.* **683**, A219 (2024).
27. Vernazza, J. E., Avrett, E. H. & Loeser, R. Structure of the solar chromosphere. III. Models of the EUV brightness components of the quiet sun. *Astrophys. J. Suppl. Ser.* **45**, 635–725 (1981).
28. Petaev, M. I. & Wood, J. A. The condensation with partial isolation (CWPI) model of condensation in the solar nebula. *Meteorit. Planet. Sci.* **33**, 1123–1137 (1998).
29. Jorge, D. M., Kamp, I. E. E., Waters, L. B. F. M., Woitke, P. & Spaargaren, R. J. Forming planets around stars with non-solar elemental composition. *Astron. Astrophys.* **660**, A85 (2022).
30. Gail, H. P. Radial mixing in protoplanetary accretion disks. IV. Metamorphosis of the silicate dust complex. *Astron. Astrophys.* **413**, 571–591 (2004).
31. Komatsu, M. et al. First evidence for silica condensation within the solar protoplanetary disk. *Proc. Natl Acad. Sci.* **115**, 7497–7502 (2018).
32. Krot, A. N. Refractory inclusions in carbonaceous chondrites: records of early solar system processes. *Meteorit. Planet. Sci.* **54**, 1647–1691 (2019).
33. Torrano, Z. A. et al. A common isotopic reservoir for amoeboid olivine aggregates (AOAs) and calcium-aluminum-rich inclusions (CAIs) revealed by Ti and Cr isotopic compositions. *Earth Planet. Sci. Lett.* **627**, 118551 (2024).
34. Sargent, B. A. et al. Dust processing and grain growth in protoplanetary disks in the Taurus–Auriga star-forming region. *Astrophys. J. Suppl. Ser.* **182**, 477–508 (2009).
35. Olofsson, J. et al. C2D Spitzer-IRS spectra of disks around T Tauri stars. IV. Crystalline silicates. *Astron. Astrophys.* **507**, 327–345 (2009).
36. Wang, Y., Ormel, C. W., Mori, S. & Bai, X.-N. Solving for the 2D water snowline with hydrodynamic simulations. Emergence of gas outflow, water cycle and temperature plateau. *Astron. Astrophys.* **696**, A38 (2025).
37. Faure, J., Fromang, S. & Latter, H. Thermodynamics of the dead-zone inner edge in protoplanetary disks. *Astron. Astrophys.* **564**, A22 (2014).
38. Yang, L. & Ciesla, F. J. The effects of disk building on the distributions of refractory materials in the solar nebula. *Meteorit. Planet. Sci.* **47**, 99–119 (2012).
39. Shu, F. H., Shang, H. & Lee, T. Toward an astrophysical theory of chondrites. *Science* **271**, 1545–1552 (1996).
40. Morbidelli, A. et al. Formation and evolution of a protoplanetary disk: combining observations, simulations, and cosmochemical constraints. *Astron. Astrophys.* **691**, A147 (2024).
41. Cridland, A. J. et al. Early planet formation in embedded protostellar disks. Setting the stage for the first generation of planetesimals. *Astron. Astrophys.* **662**, A90 (2022).
42. McClure, M. K., Dominik, C. & Kama, M. Measuring the atomic composition of planetary building blocks. *Astron. Astrophys.* **642**, L15 (2020).
43. Alexander, C. M. O. Quantitative models for the elemental and isotopic fractionations in the chondrites: the non-carbonaceous chondrites. *Geochim. Cosmochim. Acta* **254**, 246–276 (2019).
44. Grewal, D. S., Nie, N. X., Zhang, B., Izidoro, A. & Asimow, P. D. Accretion of the earliest inner Solar System planetesimals beyond the water snowline. *Nat. Astron.* **8**, 290–297 (2024).
45. Scherstén, A., Elliott, T., Hawkesworth, C., Russell, S. & Masarik, J. Hf–W evidence for rapid differentiation of iron meteorite parent bodies. *Earth Planet. Sci. Lett.* **241**, 530–542 (2006).
46. Kleine, T. et al. Hf–W chronology of the accretion and early evolution of asteroids and terrestrial planets. *Geochim. Cosmochim. Acta* **73**, 5150–5188 (2009).

Methods

System properties

The isolated single Class I protostar HOPS-315 is still embedded in a dusty protostellar envelope with a $i = 40° \pm 8°$ inclination[25] that provides a sightline down the outflow cavity wall to the hot gas accreting from the disk onto the star at a visual extinction of $A_V \approx 38$ magnitudes[17]. The central K7 protostar has a mass of $0.6\,M_{\odot}$, with an accretion luminosity $L_{acc} = 3.2\,L_{\odot}$ and stellar luminosity $L_{star} = 3.7\,L_{\odot}$, and a mass accretion rate of $\dot{M} \approx 8.5 \times 10^{-7}\,M_{\odot}\,year^{-1}$ (ref. 5). With this accretion rate, HOPS-315 should become a solar mass pre-main sequence star by 1 Myr.

The average age for a Class I protostar is 0.135 ± 0.011 Myr, equal to the sum of the half-lives of the Class 0 (0.047 ± 0.004 Myr) and Class I (0.088 ± 0.007 Myr) stages[6], which is bootstrapped from population statistics and older systems with known ages. The detection of millimetre SiO in HOPS-315's jet is more consistent with a Class 0 age[25]. Tobin et al.[47] measure an 870-μm disk dust mass of $M_{dust} = 105.6 \pm 2.0\,M_{\oplus}$ (or about $0.03\,M_{\odot}$, assuming a gas/dust ratio of 100), making HOPS-315's disk more massive than 80% of Orion Class Is and essentially average for a Class 0. However, their disk radius of $R_{disk} = 45.6 \pm 10.0$ AU is average for a Class I and smaller than 60% of Class 0 disks, suggesting that HOPS-315's disk is particularly dense and probably on the younger end of the Class I evolutionary stage.

On the basis of SiO knots in its jet, HOPS-315 has outbursting events on an approximately 50-year time frame[25]. The infrared light curve has only recently begun rising after remaining flat for two decades, but the crystalline silicate absorption features in the MIRI spectrum cannot be associated with this outburst, as they were equally strong in two Spitzer Infrared Spectrograph spectra taken in 2005, 18 years before our observations. This argues in favour of their origin in a non-transient disk structure, such as the midplane thermostat region.

Observations and data reduction

JWST. HOPS-315 was observed by JWST with the MIRI Medium-Resolution Spectrometer on 15 March 2023, through programme 1854 (PI M. K. McClure). We used a standard four-point dither pattern centred on the IRAC coordinates, with target acquisition to centre the source. The total science exposure was 222 s using the FASTR1 readout pattern. The data were processed through JWST pipeline version 1.12.3 (ref. 48), which includes the time-dependent correction for the throughput of channel 4. The calibration reference file database version 11.16.21 and jwst_1141.pmap was used, which includes revised onboard flat-field and throughput calibrations for an absolute flux calibration accuracy estimate of 5.6 ± 0.7% (ref. 49). We performed the standard steps in the JWST pipeline to process the data from the 3D ramp format to the cosmic ray corrected slope image. A dedicated sky observation taken nearby was used to subtract the astrophysical background from the flux of the target after the 'Level 1' run, whereas further processing of the 2D slope image for assigning pixels to coordinates, flat fielding and flux calibration was also conducted using standard steps in the 'Level 2' data pipeline calwebb_spec2. We ran the 'Stage 3' pipeline to build the calibrated 2D IFU slice images in the 3D datacube. The 3D cube of the final pipeline processed product was built with the outlier bad pixel rejection step turned off, as it overcorrected pixels and removed target flux.

The JWST-NIRSpec/IFU observations were taken on 15 September 2023, using the G235H and G395H filters. We used a four-point cycling dither pattern, starting from position 6. The integration time was 233 s with an NRSIRS2RAPID readout pattern. We did not take a background frame, but because HOPS-315 resides in a region with bright backgrounds, we corrected for stray light in the failed open MSA shutters by taking a leakcal observation at each dither position. We used the standard 3D cube taken from the Mikulski Archive for Space Telescopes (MAST) archive using the calibration reference file database version 11.17.2 and jwst_1130.pmap.

For both MIRI and NIRSpec, the spectrum in each subchannel was extracted using a conical extraction with a circular aperture whose radius was 2.5 times the resolution element at each wavelength, with a minimum radius of 1.25 arcsec.

ALMA. HOPS-315 was observed with ALMA located on Llano de Chajnantor in Northern Chile on 19 November 2023. The observations were conducted in three consecutive executions with a maximum baseline length of 6,582 m for a total on-source time of roughly 106 min. The monitored quasar J0423−0120 was the bandpass and absolute flux calibrator in the first and second execution and J0538−4405 was the bandpass and flux calibrator during the third execution. The phase calibrator was J0527+0331 in all executions. The central frequency of the observations was roughly 344.8 GHz (Band 7), covering the CO $J = 3 - 2$ (345.795990 GHz), SiO $v = 0, J = 8 - 7$ (347.330579 GHz) and SO $8_8 - 7_7$ (344.310612 GHz) transitions. The absolute flux density uncertainty in Band 7 is expected to be roughly 5%.

The data were reduced and imaged using the ALMA calibration pipeline version 2023.1.0.124 in CASA v.6.5.4.9 (ref. 50). This included self-calibration on the continuum data after which the phase and amplitude solutions were applied to the line data and continuum subtraction based on a fit to the line-free continuum regions in uv-space. The molecular lines were imaged using a robust parameter of 0.5 (resulting in a beam size of 0.06″ × 0.05″), an image size of 2,250 × 2,250 and a pixel size of 0.0095″. A channel spacing of 0.4 km s^{-1} was used for SiO and 0.85 km s^{-1} for CO and SO. A primary beam correction was applied to all images. The rms per channel is roughly 1.4 mJy per beam for SiO, 1.0 mJy per beam for CO and 0.92 mJy per beam for SO. The maximum resolvable scale is 0.8″. We measure a local system velocity of $\upsilon_{system} = 9.68 \pm 0.19$ km s^{-1} in the LSRK velocity reference frame by fitting a Gaussian to the narrow, central SO component. This value is consistent with the $\upsilon_{system} = 9.9$ km s^{-1} found in ref. 25 using their peak $C^{18}O$ emission with 1.4 km s^{-1} resolution.

The size of the infrared SiO emitting region can be constrained from the ALMA non-detection of SiO at the stellar position. On the basis of the column density derived from the JWST SiO absorption, the observed millimetre transition should be optically thick. A reservoir of SiO at the measured temperature of 488 K with a radius of 10 AU (half the ALMA beam) should have been easily detected, both in the millimetre SiO image and with a narrow central component, similar to that seen in our SO spectrum and the $C^{18}O$ from ref. 25. The rms in the SiO image is 6.34 K per channel at the native velocity resolution of 0.4 km s^{-1}, so the JWST SiO should arise within a circular area with a radius of 2.2 AU to not be detected in the ALMA observations, assuming a 3σ noise limit. If the emitting area of the infrared SiO is an annulus rather than a circular area, the area would be equivalent to a circle with 2.2 AU radius.

We calculated CO and SiO column densities from the integrated flux extracted in a 0.2″ radius aperture centred 0.32″ off-source along the jet, within the spectral velocity range of the blueshifted SiO jet (−75.6 to −50.7 km s^{-1}). The aperture was chosen to match the brightest knot in the H_2 1-0 S(1) jet emission found by Vleugels et al.[18]. We assumed gas at 150 K, following Section 3.3 of ref. 25, with molecular line parameters from the Cologne Database for Molecular Spectroscopy[51].

Solid-state fitting

HOPS-315's JWST spectrum encompasses numerous solid-state absorption features (Fig. 2), including ices and amorphous silicates, which may arise in both the protostellar envelope and the young disk. The three bands of H_2O ice at 3, 6 and 12 μm trace temperatures $T < 130$ K. Two CO_2 ice features appear at 4.27 and 15.30 μm; the profile of the latter is consistent with CO_2 ice trapped in an H_2O ice matrix[52], rather than pure CO_2 ice, suggesting temperatures between the CO_2 sublimation temperature of $T = 70$ K and the H_2O crystallization temperature around 130 K. The CO ice absorption at 4.7 μm traces material at $T < 20$ K. Superimposed on the broad amorphous silicate features from 8–10 μm and

16–21 μm, we see sharp absorption features indicative of crystalline silicates, which can only be produced in the hot inner regions of the young disk above about 800 K. To identify the minerals with the most statistically significant contribution to these sharp features, we analyse the 5–28-μm region.

To isolate the crystalline silicate features, we first fit a fourth-order polynomial to the regions indicated in the figure, fitting slightly above the data continuum to leave room for the optical depth spectra, which have some non-zero baseline absorption. This continuum was used to calculate the optical depth, $\tau = -\ln(F_{\text{spectrum}}/F_{\text{continuum}})$. This step has a large systemic uncertainty that is influenced by the source geometry and temperature gradient, giving rise to the strong continuum. Extensive radiative transfer modelling, beyond the scope of this work, is required to fully account for the systematic uncertainty on the optical depth spectrum.

We used the OPTOOL software package[53] to calculate opacities from laboratory optical constants for the following solids: H_2O and CO_2 ice[52], interstellar silicates[54], the crystalline silicates forsterite (Mg_2SiO_4 (ref. 55)), enstatite ($MgSiO_3$ (ref. 56)) and silica (SiO_2 (ref. 57)) and minerals that contribute to CAIs, such as corundum (α-Al_2O_3 (ref. 58)), hibonite ($CaAl_{12}O_{19}$ (ref. 59)), gehlenite ($Ca_2Al_2SiO_7$ (ref. 60)), perovskite ($CaTiO_3$ (ref. 61)) and spinel ($MgAl_2O_4$ (ref. 58)). We corrected for grain shape and size effects with a continuous distribution of ellipsoids of size distribution $n(a) = n_0 a^{-3.5}$, with $0.005\ \mu\text{m} \le a \le a_{\text{max}}$. For the ice mixture, the $a_{\text{max}} = 1\ \mu\text{m}$, whereas for the refractory minerals, we assumed $a_{\text{max}} = 0.25\ \mu\text{m}$, as direct condensates initially form smaller grains and such grains produce sharper features than larger grains. The temperatures of the laboratory refractory minerals were between 273 and 300 K; higher temperatures shift the peak wavelength positions, but temperature-dependent datasets were only available for a small subset of the tested minerals. The refractive index for the ice was calculated from an absorbance spectrum of H_2O:CO_2 (10:1) ice mixture at 130 K from ref. 52, using the NKABS code[62], an ice thickness of 0.5 μm and $n_0 = 1.32$. The last if these accounts for the refractive profile below 2 μm, at which the laboratory data begin. The 10:1 mixture was the only binary mixture of these ice species available at present in the Leiden Ice Database for Astrochemistry (LIDA)[62]; there were no other strong ice components present in this part of the MIRI spectrum. For each mineral, we calculated the optical depth spectrum from the opacities. For minerals with several polymorphs, for example, silica and enstatite, we considered only the most common polymorphs found in protoplanetary disks by previous authors[34,35]. To represent interstellar silicates, we used the Galactic Center Source (GCS3) template[54].

We performed ENIIGMA fits on the MIRI range of HOPS-315, between 7.7 and 27.7 μm, at which the strong silicate features are visible. The ENIIGMA methodology, described fully in ref. 63, uses genetic modelling algorithms to find the global minimum fit from a linear combination of the infrared optical depth spectra calculated from the opacities described above. We performed fits with the ice blend, interstellar silicates and all of the refractory mineral components; however, our results showed that only the five minerals discussed in the main text (the crystalline silicates) were statistically significant. We refer to this model as 'M5(w)' in Extended Data Table 1. We also calculated the confidence intervals on the abundance of each mineral with ENIIGMA, with the 3σ confidence level reported in Extended Data Table 1 and corner plot reported in the Supplementary Information (Supplementary Fig. 1). The 3σ confidence intervals are never below 0, which indicates that all of the listed minerals improve the fit.

However, the quality of the silica and forsterite fits is affected by the slope of the continuum fit from 11 to 15 μm, under the 12.5-μm crystalline silica feature. This continuum could be affected by a temperature gradient in the H_2O:CO_2 ice mixture, which would shift the peak of the ice from 11.8 μm either shorter or longer wavelengths; this would affect the fit to the 12.5-μm silica feature and the 11.3-μm forsterite feature. Exploring the presence of temperature gradients requires a different modelling set-up that will be explored in a future work.

To explore the systematic uncertainty in the silica abundance, we produced a second fit between 7.75 and 28.00 μm without silica, as shown in Extended Data Fig. 2. This four-component, wide model ('M4(w)') reproduces the 20-μm features marginally better than our standard model, but is a poorer match to the 8.0–9.5-μm and 11.5–13.0-μm slopes. A quality assessment using the reduced chi-squared (χ_r^2) and Akaike information criterion (AIC) metrics, as described in the Supplementary Information, indicates that, over the 7.75–28.00 μm range, the M5(w) model with silica provides a better fit than the M4(w) model without silica by the χ_r^2 metric ($\chi_r^2 = 7.28$ versus 8.13, respectively) but not by a statistically significant amount according to the AIC metric (AIC = 17.29 versus 16.14, respectively), as the difference in the AIC is less than 2 (ref. 64).

Because the 10-μm and 20-μm silicate complexes trace different radial locations when seen in emission[11,34,35], we tested whether the silica model might be robust when limiting the fits to the three silica features at 8.2, 9.0 and 12.5 μm with a shorter wavelength range from 7.75 to 13.20 μm, as shown in Extended Data Fig. 3. For the shorter wavelengths, the model with silica, 'M5(s)', is statistically preferred over the model without silica, 'M4(s)', with both metrics, as $\chi_r^2 = 6.71$ versus 14.37 and AIC = 16.72 versus 22.37, with ΔAIC > 2. Specifically, the absorption from 8–9 μm is improved, along with the shape of the absorption at 12.5 μm. Therefore, we conclude that crystalline silica is (tentatively) present in the 10-μm complex, given our modelling approach and the laboratory data to which we have access, on the basis of the statistically better fit to the 8–9-μm and 12–13-μm absorption. Future modelling that includes temperature gradients in the silicates and ices and tests to rule out further, less common, polymorphs of enstatite and silica would confirm this silica detection.

Slab model fitting

To analyse the molecular features, we use the local thermodynamic equilibrium (LTE) slab models of ref. 65, adapted from the LTE emission models of refs. 66,67. These models assume that the line absorption comes from a region with a single temperature and density, whereas disks have gradients in both parameters. However, comparison between slab models and full, 2D chemical models of the same disk[26,68] shows that, for a given molecular band, the slab model closely approximates the mean temperature and density of that band's emitting area in the 2D model, although it may not recover values at either extreme of the gradient. To compensate for this effect, we fit each molecular band of each species individually, as they probably trace different disk regions.

Our models use molecular spectroscopy data from the LAMDA and HITRAN databases to compute the level populations, assuming they are in LTE with a single excitation temperature T_{ex}. The partition functions needed for the model calculations are taken from the TIPS database. The LTE assumption should be robust for the dense, collisionally dominated disk environment. We compute the line centre optical depth of each transition assuming a single column density, N, and linewidth, ΔV, following (ref. 67). A synthetic optical depth spectrum is created by sampling the lines at high resolution ($R = 10^6$), assuming a Gaussian line profile of full width at half maximum ΔV. For the absorption features, we immediately convolve with the instrument response.

For the CO overtone emission feature, we correct the emission for extinction assuming a visual extinction $A_{\text{V}} = 38$ from ref. 17 using the extinction curve of ref. 69 and then convert the optical depth spectrum $\tau(\lambda)$ to flux units through $F(\lambda) = \pi \left(\frac{R}{d}\right)^2 B_\nu(T_{\text{ex}})\,(1 - \mathrm{e}^{-\tau(\lambda)})$, in which R is the characteristic radius of the emitting slab, $d = 420$ pc is the distance to the source, B_ν is the Planck function and τ is the line optical depth. We warn that the characteristic radius R is simply a scaling factor for the emitting area of the cylindrical slab, which is assumed to represent the emission, and should not be interpreted as a disk radius without constraints on the geometry of the emitting region.

To fit the observed molecular absorption features, we fit a baseline to the observed spectrum using a guided cubic spline and convert from flux to optical depth units through $\tau_{\mathrm{obs}} = -\log(F_{\mathrm{obs}}/F_{\mathrm{baseline}})$. Although JWST cannot velocity-resolve these lines, our high SNR constrains ΔV through the amplitude and line profile shapes in cases in which the absorption lines have sufficient optical depth. Similarly, we can constrain large velocity shifts of the molecular bands, finding good agreement assuming rest-frame wavelengths in the barycentric system or blueshifted by 20–30 km s^{-1} with respect to the ALMA source velocity of +9.68 km s^{-1} in the LSRK velocity frame. To determine the best-fit values for each band, we use a Bayesian analysis in which the likelihood assumes the observed optical depth to have a Gaussian noise of 0.01τ and a uniform prior over the model parameters N, ΔV and T_{ex}. In this case, the likelihood function is $\frac{1}{2}\chi^2$ and finding the best-fit model is effectively a χ^2 minimization. We use the Markov chain Monte Carlo sampling method from the Python package emcee[70] to sample the posterior probability. Corner plots for all modelled bands are given in Supplementary Figs. 2–10,12.

We calculated the disk radii at which each band absorbs from the ΔV, assuming that the linewidth is Doppler broadened, $\Delta V = v_{\mathrm{Doppler}}\sin(i)$, using $i = 40°$. We consider that v_{Doppler} is mostly because of Keplerian motion of the disk, $v_{\mathrm{Keplerian}} = \sqrt{(GM_{*}R_{\mathrm{disk}}^{2})/(R_{\mathrm{disk}}^{2} + z_{\mathrm{disk}}^{2})^{3/2}}$. Extended Data Table 2 reports a range of radii for two limiting cases: one in which $z_{\mathrm{disk}}/R_{\mathrm{disk}} = 0.2$, which is the approximate vertical height of the disk photosphere in ref. 14, and the other $z_{\mathrm{disk}}/R_{\mathrm{disk}} = 0$, at the disk midplane, which provides an outer limit despite being unphysical given the optical depth of the inner disk. Increasing the absorption height pushes the radius closer to the star. Turbulent contributions to the linewidth would push the radii farther out in the disk. Typical values for turbulence in the inner disk range from 7 to 15 km s^{-1} in hot, approximately 1,500 K H_2O and CO overtone emission[71], but our temperatures are substantially less than that for all absorption bands.

To determine whether the SiO absorption originates in the jet, we fit a Gaussian profile to bright and well-resolved $v = 1 - 0$ transitions of SiO between 7.9 and 8.5 μm and compute the velocity offset from the barycentric rest-frame wavelength of each transition, the results of which are shown in Extended Data Fig. 1. The mean velocity offset is 6.7 ± 1.2 km^{-1}, with the uncertainty calculated from the standard error in the mean of σ/N, with N the number of lines fit. Converting to the LSRK reference frame, this is -10.6 ± 1.2 km s^{-1}, consistent with an infrared SiO origin in the disk rather than in the high-velocity jet.

Apart from H_2, the only detected molecular emission is the CO overtone band at 2.3 μm, which we similarly fit with a Bayesian method. However, the emitting radius R is an extra parameter and ΔV is fixed to the best-fit value of the ^{12}CO absorption of 37.7 km s^{-1}, necessitated by severe line blending in the bandhead. This value is physically motivated if the overtone emission probes the outflowing CO launched from the inner edge of the thermostat region.

H_2O. Four bands of gaseous H_2O are present in these spectra, three of which are fit in Extended Data Fig. 4. The ro-vibrational water bands at 2.5–3.0 μm and 5–6 μm and the rotational water at 15–17 μm all trace a reservoir of warm gas between 400 and 525 K and column densities of 10^{18}–10^{19} cm^{-2}. The two colder bands trace higher column densities between 0.3. and 0.6 AU of the star. By contrast, the hotter band traces less dense material nearly 11 AU away but closer to the disk photosphere, based on its weaker optical depths.

C_2H_2 and HCN. The absorption bands of C_2H_2 and HCN gas both probe warm gas near 0.1 AU from the star at temperatures between 500 and 700 K but at columns of 10^{15}–10^{16} cm^{-2}, shown in Extended Data Fig. 5. Despite the excellent SNR of these data, there are large uncertainties on the C_2H_2 fit in particular, owing to the weakness of the features. Their weak optical depth indicates that these molecules probably originate near the disk photosphere, consistent with their predicted location from 2D disk chemical models for emission spectra[26].

CO_2. The 4.27-μm gas absorption traces higher temperatures and lower column densities than the 15.3-μm band, 351 K and 10^{17} cm^{-2} at 0.40 AU versus 124 K and 10^{19} cm^{-2} at 18.11 AU, respectively (Extended Data Fig. 6), opposite to the pattern seen for water. This may indicate that more of the carbon budget is carried by the CO_2 gas at 18 AU, sublimated from the H_2O:CO_2 ice, whereas a larger fraction of the gaseous carbon at 0.40 AU may be carried by CO.

CO. The CO fundamental gas band shows several absorption components (Extended Data Fig. 7). We fit the unblended ^{13}CO component and a single ^{12}CO component at 646 K and 9.14×10^{17} cm^{-2} and 1,181 K and 7.39×10^{18} cm^{-2}, respectively. The temperature of the ^{12}CO is consistent with gas at the upper, low-density end of the silicate sublimation front in mature protoplanetary disks[12], consistent with the radius of 0.16 ± 0.01 AU implied by its best-fitting ΔV value. Converting the ^{13}CO column, located at 0.17 ± 0.02 AU, to ^{12}CO, assuming the interstellar ratio[72], yields a column of 6.30×10^{19} cm^{-2}, confirming that these CO components probe downward through vertical structure in the temperature inversion layer at similar radii.

However, our fits also demonstrate the presence of further, optically thick temperature components, both a warm ^{12}CO not found by our models and, in the residuals of this fit, a missing cold ^{12}CO component, $T \le 40$ K, that may correspond to the disk wind seen in ALMA ^{12}CO emission or the protostellar hot core[73] (see Extended Data Fig. 7 and Supplementary Fig. 11). However, the high optical depth of the cold CO lines is difficult to reconcile with the observations without a very large ΔV that is ruled out by the line profiles. This suggests that the covering fraction of the continuum against which the hot and cold components are absorbing may be spatially different owing to the geometry of the system and, therefore, the optical depth of the cold component may be lower than we derive using the present continuum. Higher temperature outflowing material may potentially contribute to the CO overtone emission at 2.3 μm; the best-fitting emitting radius of 0.54 AU, high temperature of 3,775 K and high density of 2.40×10^{21} cm^{-2} suggest that it traces not only the superheated disk atmosphere above the inversion layer but also the same outflowing material probed by the H_2 emission seen by ref. 18. However, because the CO gas and outflow structure is not the scientific focus of this paper, we leave a more complex model of the different components to a future work.

Disk silicate retention calculation

The column densities of CO and SiO in the jet are $N_{\mathrm{CO,jet}} = 1.52 \times 10^{17}$ cm^{-2} and $N_{\mathrm{SiO,jet}} = 2.78 \times 10^{14}$ cm^{-2}, respectively, leading to $(\mathrm{Si/C})_{\mathrm{jet}} = 2.4 \times 10^{-3}$, or only 1.7% of the expected Si, assuming cosmic Si/C. Because the jet abundances should reflect the abundance at the jet launching radius in the disk, which is just interior to the silicate sublimation radius, the silicon depletion of the jet suggests that 98.3% of the silicon is being retained in the disk as condensed silicates, whereas the carbon is fully launched into the jet as CO gas.

Data availability

The original data are publicly available through the JWST MAST archive and ALMA archives. Our version of the 1D extracted spectra is on *Zenodo* at https://doi.org/10.5281/zenodo.15556630 (ref. 74).

Code availability

The solid-state fitting code ENIIGMA developed by W.R.M.R. is publicly available on GitHub: https://github.com/willastro/ENIIGMA-fitting-tool. The slab model used in this work is a private code developed by L.F. and collaborators, based on the private code developed by B. Tabone for emission line slab models. It is available from L.F. on request.

47. Tobin, J. J. et al. The VLA/ALMA Nascent Disk and Multiplicity (VANDAM) survey of Orion protostars. II. A statistical characterization of Class 0 and Class I protostellar disks. *Astrophys. J.* **890**, 130 (2020).
48. Bushouse, H. et al. JWST Calibration Pipeline. *Zenodo* https://doi.org/10.5281/zenodo.6984365 (2023).
49. Argyriou, I. et al. JWST MIRI flight performance: the Medium-Resolution Spectrometer. *Astron. Astrophys.* **675**, A111 (2023).
50. McMullin, J. P., Waters, B., Schiebel, D., Young, W. & Golap, K. CASA architecture and applications. *Astron. Soc. Pac. Conf. Ser.* **376**, 127 (2007).
51. Müller, H. S. P., Schlöder, F., Stutzki, J. & Winnewisser, G. The Cologne Database for Molecular Spectroscopy, CDMS: a useful tool for astronomers and spectroscopists. *J. Mol. Struct.* **742**, 215–227 (2005).
52. Ehrenfreund, P., Boogert, A. C. A., Gerakines, P. A., Tielens, A. G. G. M. & van Dishoeck, E. F. Infrared spectroscopy of interstellar apolar ice analogs. *Astron. Astrophys.* **328**, 649–669 (1997).
53. Dominik, C., Min, M. & Tazaki, R. OpTool: command-line driven tool for creating complex dust opacities. Astrophysics Source Code Library, record ascl:2104.010 (2021).
54. Kemper, F., Vriend, W. J. & Tielens, A. G. G. M. The absence of crystalline silicates in the diffuse interstellar medium. *Astrophys. J.* **609**, 826–837 (2004).
55. Sogawa, H. et al. Infrared reflection spectra of forsterite crystal. *Astron. Astrophys.* **451**, 357–361 (2006).
56. Jaeger, C. et al. Steps toward interstellar silicate mineralogy. IV. The crystalline revolution. *Astron. Astrophys.* **339**, 904–916 (1998).
57. Sargent, B. A. et al. Silica in protoplanetary disks. *Astrophys. J.* **690**, 1193 (2008).
58. Zeidler, S., Posch, T. & Mutschke, H. Optical constants of refractory oxides at high temperatures. Mid-infrared properties of corundum, spinel, and α-quartz, potential carriers of the 13 μm feature. *Astron. Astrophys.* **553**, A81 (2013).
59. Mutschke, H., Posch, T., Fabian, D. & Dorschner, J. Towards the identification of circumstellar hibonite. *Astron. Astrophys.* **392**, 1047–1052 (2002).
60. Mutschke, H. et al. Steps toward interstellar silicate mineralogy. III. The role of aluminium in circumstellar amorphous silicates. *Astron. Astrophys.* **333**, 188–198 (1998).
61. Posch, T. et al. Infrared properties of solid titanium oxides: exploring potential primary dust condensates. *Astrophys. J. Suppl. Ser.* **149**, 437–445 (2003).
62. Rocha, W. R. M. et al. LIDA: the Leiden Ice Database for Astrochemistry. *Astron. Astrophys.* **668**, A63 (2022).
63. Rocha, W. R. M., Perotti, G., Kristensen, L. E. & Jørgensen, J. K. Fitting infrared ice spectra with genetic modelling algorithms. Presenting the ENIIGMA fitting tool. *Astron. Astrophys.* **654**, A158 (2021).
64. Burnham, K. P. & Anderson, D. R. *Model Selection and Multimodel Inference: A Practical information-theoretic Approach* (Springer, 2002).
65. Francis, L. et al. JOYS: MIRI/MRS spectroscopy of gas-phase molecules from the high-mass star-forming region IRAS 23385+6053. *Astron. Astrophys.* **683**, A249 (2024).
66. Grant, S. L. et al. MINDS. The detection of $^{13}CO_2$ with JWST-MIRI indicates abundant CO_2 in a protoplanetary disk. *Astrophys. J. Lett.* **947**, L6 (2023).
67. Tabone, B. et al. A rich hydrocarbon chemistry and high C to O ratio in the inner disk around a very low-mass star. *Nat. Astron.* **7**, 805–814 (2023).
68. Kospal, Á. et al. JWST/MIRI spectroscopy of the disk of the young eruptive star EX Lup in quiescence. *Astrophys. J. Lett.* **945**, L7 (2023).
69. Pontoppidan, K. M., Evans, N., Bergner, J. & Yang, Y.-L. A constrained dust opacity for models of dense clouds and protostellar envelopes. *Res. Notes AAS.* **8**, 68 (2024).
70. Foreman-Mackey, D., Hogg, D. W., Lang, D. & Goodman, J. emcee: the MCMC hammer. *Publ. Astron. Soc. Pac.* **125**, 306 (2013).
71. Carr, J. S., Tokunaga, A. T. & Najita, J. Hot H_2O emission and evidence for turbulence in the disk of a young star. *Astrophys. J.* **603**, 213–220 (2004).
72. Wilson, T. L. Isotopes in the interstellar medium and circumstellar envelopes. *Rep. Prog. Phys.* **62**, 143–185 (1999).
73. Thi, W. F., van Dishoeck, E. F., Pontoppidan, K. M. & Dartois, E. Evidence for episodic warm outflowing CO gas from the intermediate-mass young stellar object IRAS 08470–4321. *Mon. Not. R. Astron. Soc.* **406**, 1409–1424 (2010).
74. McClure. JWST data from McClure et al. (2025). *Zenodo* https://doi.org/10.5281/zenodo.15556630 (2025).

Acknowledgements This work is based in part on observations made with the NASA/ESA/CSA JWST. The data were obtained from the Mikulski Archive for Space Telescopes (MAST) at the Space Telescope Science Institute, which is operated by the Association of Universities for Research in Astronomy, Inc., under NASA contract NAS 5-03127 for JWST. These observations are associated with programme no. 1854. This paper makes use of the following ALMA data: ADSJAO.ALMA#2023.A.00009.S. ALMA is a partnership of the ESO (representing its member states), NSF (USA) and NINS (Japan), together with NRC (Canada), MOST and ASIAA (Taiwan) and KASI (Republic of Korea), in cooperation with the Republic of Chile. The Joint ALMA Observatory is operated by ESO, auI/NRAO and NAOJ. The National Radio Astronomy Observatory is a facility of the National Science Foundation operated under cooperative agreement by Associated Universities, Inc. E.F.v.D., L.F. and W.R.M.R. acknowledge support from the European Research Council (ERC) under the European Union's Horizon 2020 research and innovation programme (grant agreement no. 101019751 MOLDISK), from the TOP-1 Dutch Research Council (NWO) grant 614.001.751 and from the Danish National Research Foundation through the Center of Excellence 'InterCat' (grant agreement no. DNRF150). E.B. acknowledges support from NASA XRP #80NSSC24K0149. E.D. and J.A.N. acknowledge support from the French Programme National 'Physique et Chimie du Milieu Interstellaire' (PCMI) of the CNRS/INSU with the INC/INP, co-funded by the CEA and the CNES. D.H. is supported by a Center for Informatics and Computation in Astronomy (CICA) grant and grant number 110J0353I9 from the Ministry of Education of Taiwan. D.H. also acknowledges support from the National Science and Technology Council, Taiwan (grant nos. NSTC111-2112-M-007-014-MY3, NSTC113-2639-M-A49-002-ASP and NSTC113-2112-M-007-027).

Author contributions M.K.M., M.v.t.H., E.B., D.H., E.F.v.D., J.A.N., D.Q. and E.D. contributed to the JWST proposal. M.v.t.H., E.B. and M.K.M. contributed to the ALMA proposal. M.K.M., J.A.S. and M.v.t.H. reduced the JWST NIRSpec/MIRI and ALMA data, respectively. M.K.M., M.v.t.H., E.B., L.F. and W.R.M.R. designed the analysis plan. L.F. and W.R.M.R. designed and executed the JWST gas and solids modelling, with ancillary analysis by M.K.M. and input from E.F.v.D. M.v.t.H. and E.B. designed and executed the ALMA analysis. J.H.B. provided reformatted molecular data for the SiO band. M.K.M. wrote most of the main text. M.v.t.H., L.F., W.R.M.R. and M.K.M. wrote parts of the Methods and Supplementary Methods sections. All authors participated in discussion of the observations, interpretation of the results and commented on the submitted draft.

Competing interests The authors declare no competing interests.

Additional information

Supplementary information The online version contains supplementary material available at https://doi.org/10.1038/s41586-025-09163-z.

Correspondence and requests for materials should be addressed to M. K. McClure.

Peer review information *Nature* thanks Fred Ciesla and the other, anonymous, reviewer(s) for their contribution to the peer review of this work.

Reprints and permissions information is available at http://www.nature.com/reprints.

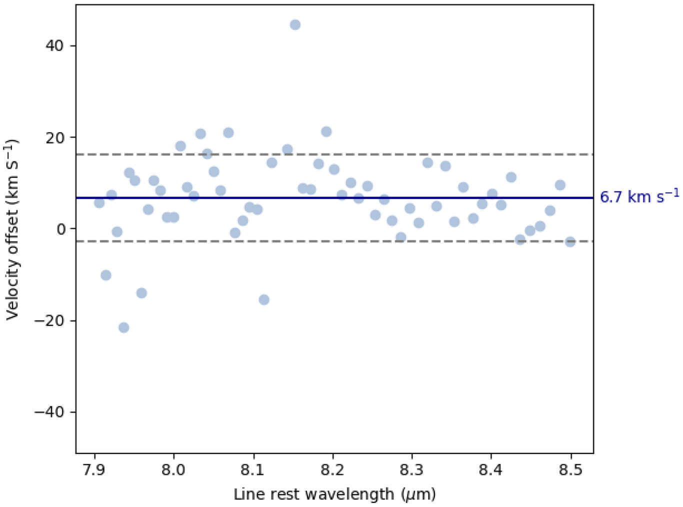

Extended Data Fig. 1 | Velocity fit to SiO band. The offset of individual SiO v = 1-0 lines (circles) from their rest-frame wavelength, as determined by a Gaussian fit, is shown between 7.9 and 8.5 μm. The mean velocity offset and mean plus or minus one standard deviation are shown by the dark blue and dashed horizontal lines, respectively. The barycentric reference frame is offset from LSRK by −17.3 km s^{-1}.

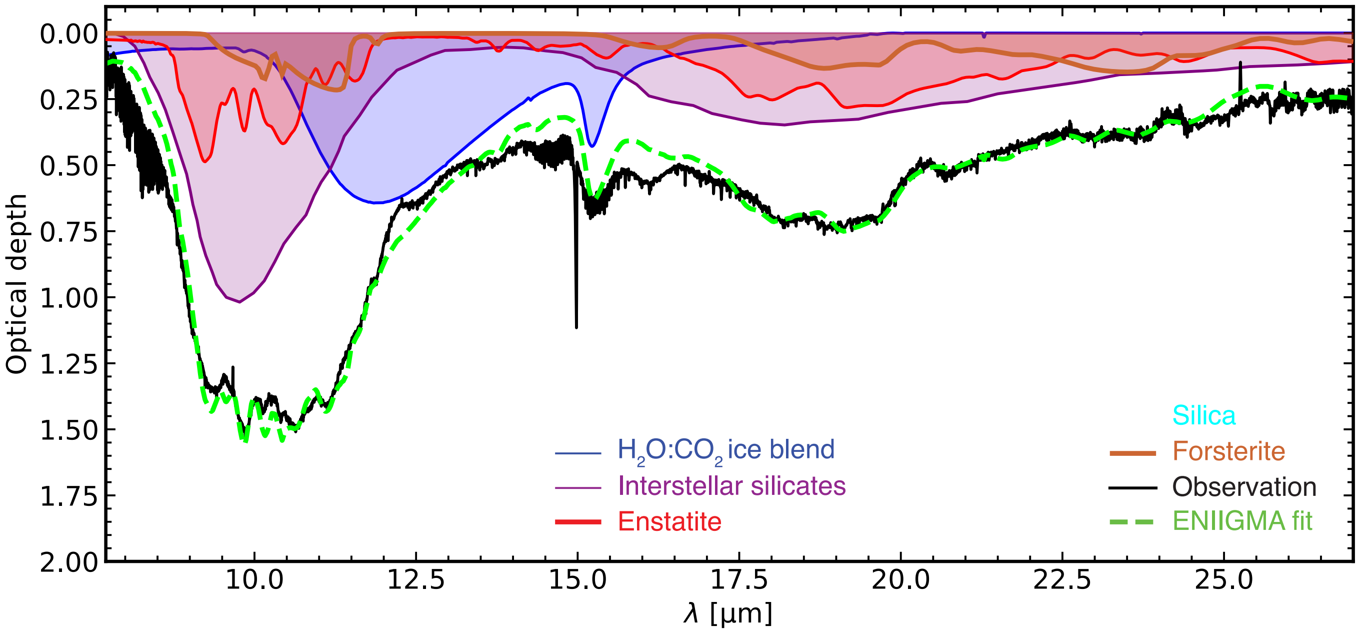

Extended Data Fig. 2 | ENIIGMA fit without silica over the whole wavelength range, M4(w).

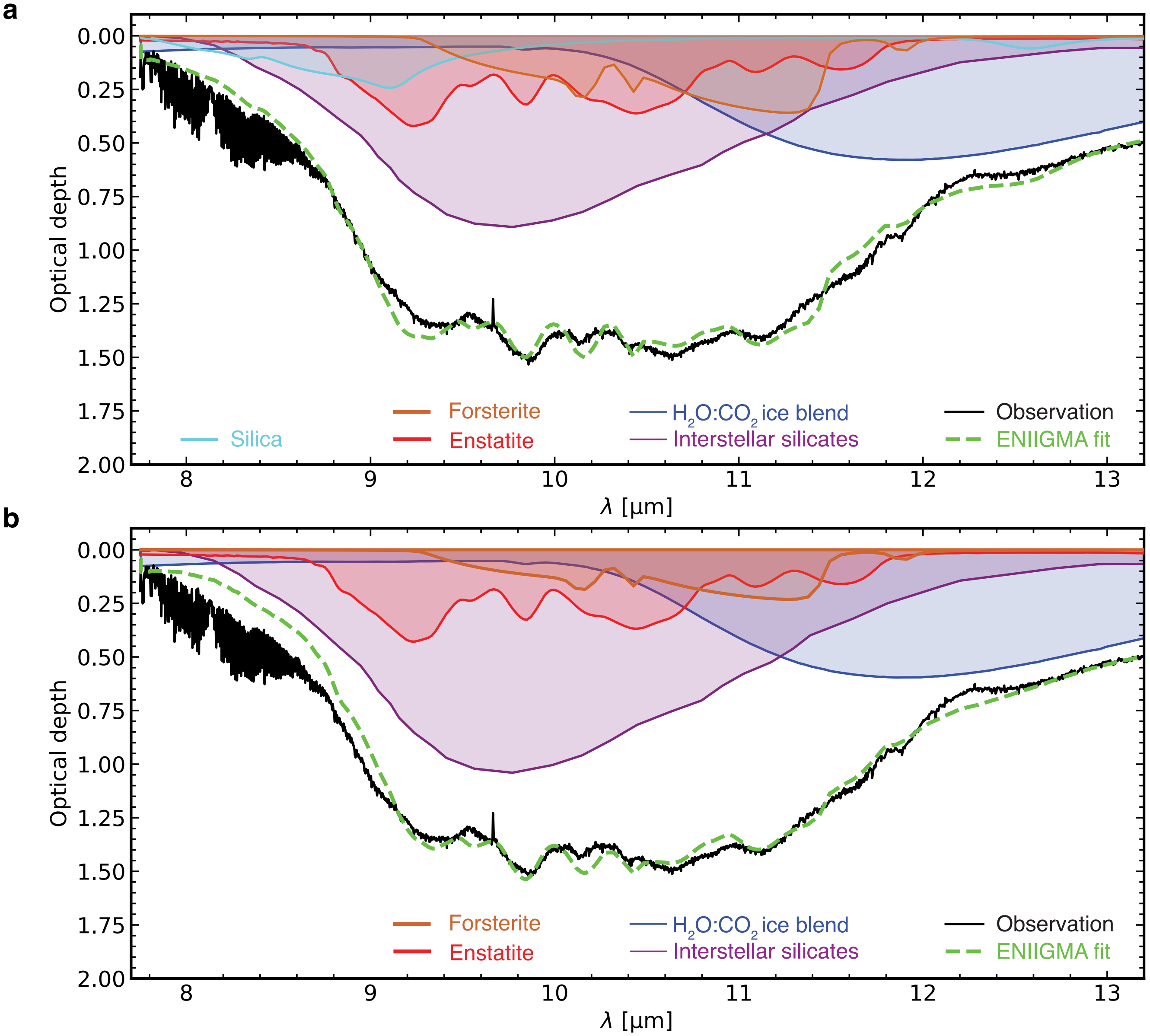

Extended Data Fig. 3 | Comparison of ENIIGMA fit with and without silica. a, Model with silica (M5(s)) over the 7.75–13.20-μm range. **b**, Model without silica (M4(s)). Silica improves the fit in a statistically significant way from 8 to 9 μm and at 12.5 μm.

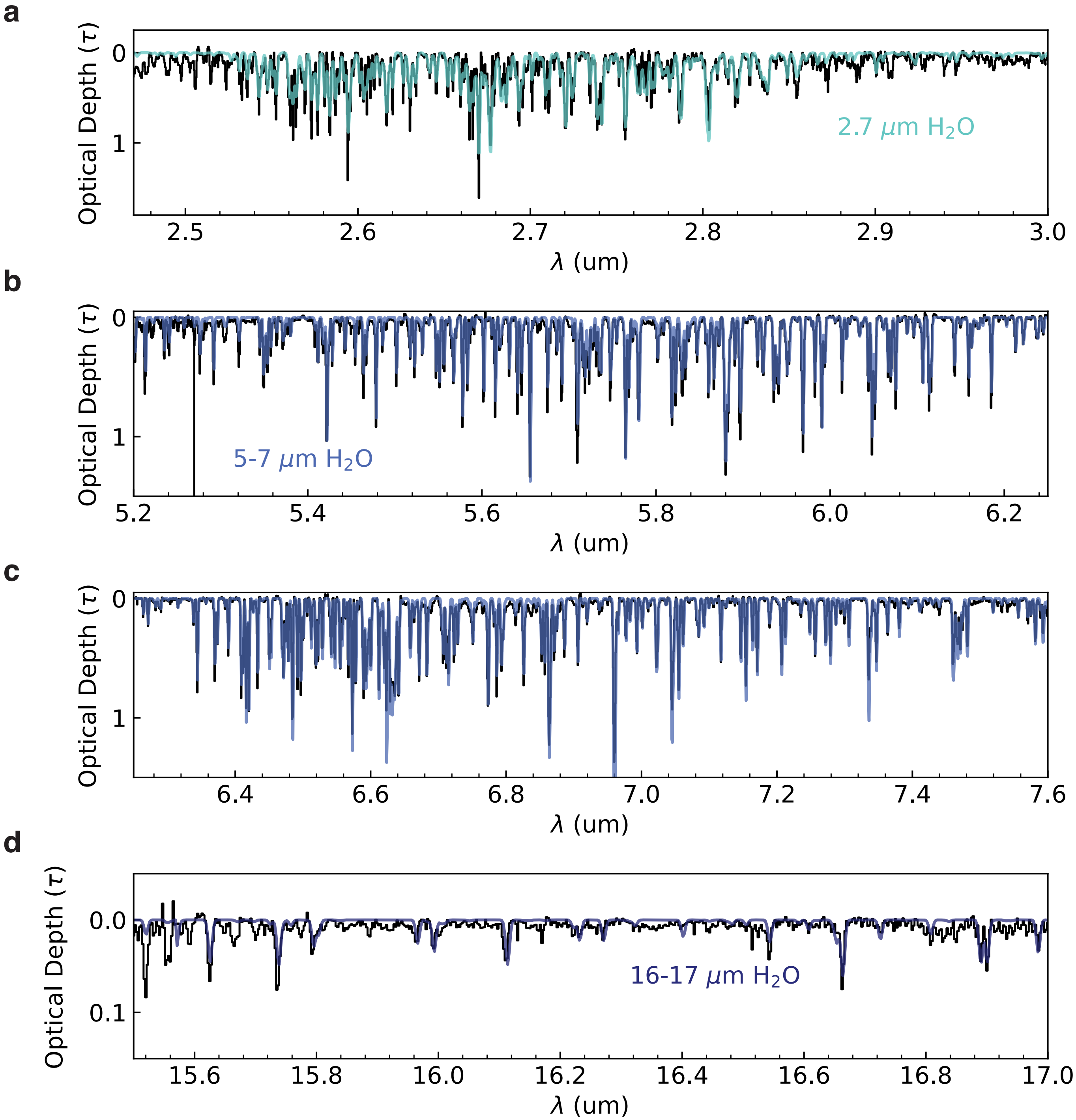

Extended Data Fig. 4 | Slab model fits to the H_2O gas-phase absorption bands. **a**, The 3-µm band. **b**,**c**, The 6–8-µm band. **d**, The 17-µm band.

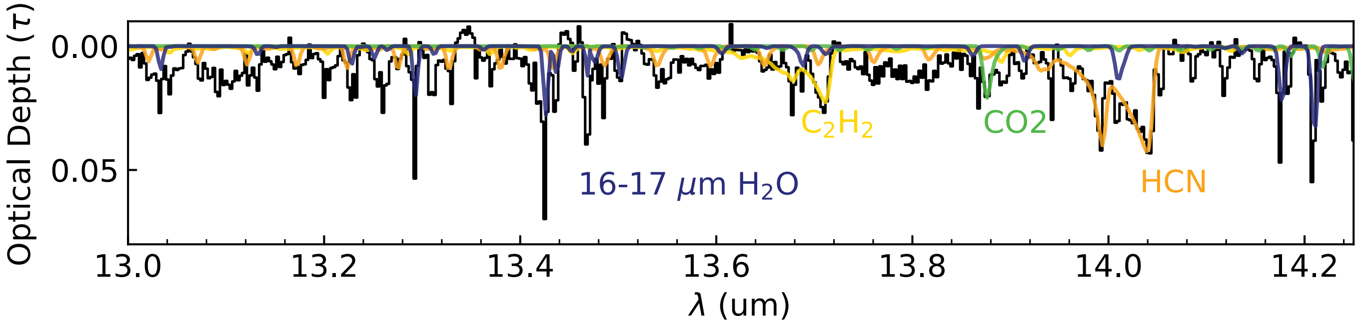

Extended Data Fig. 5 | Slab model fits to the C_2H_2 and HCN gas-phase absorption bands.

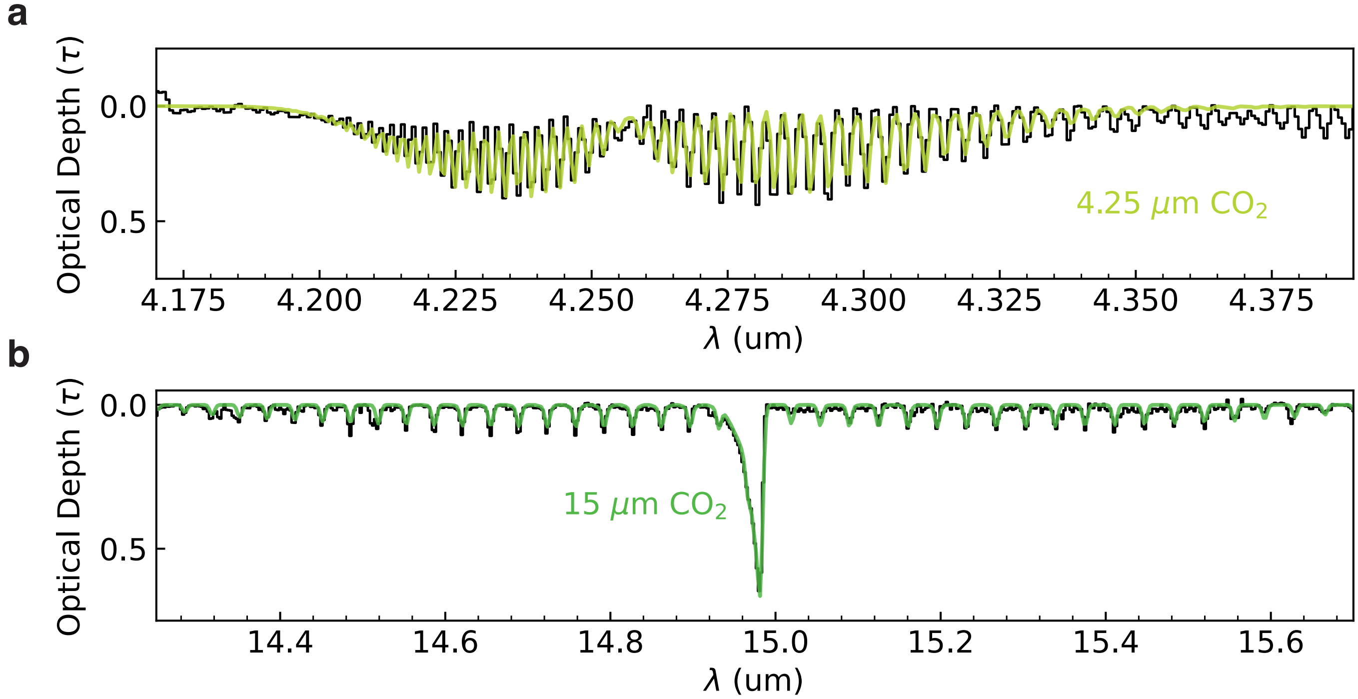

Extended Data Fig. 6 | Slab model fits to the CO_2 absorption bands. a, The 4.27-µm band. **b**, The 15.3-µm band.

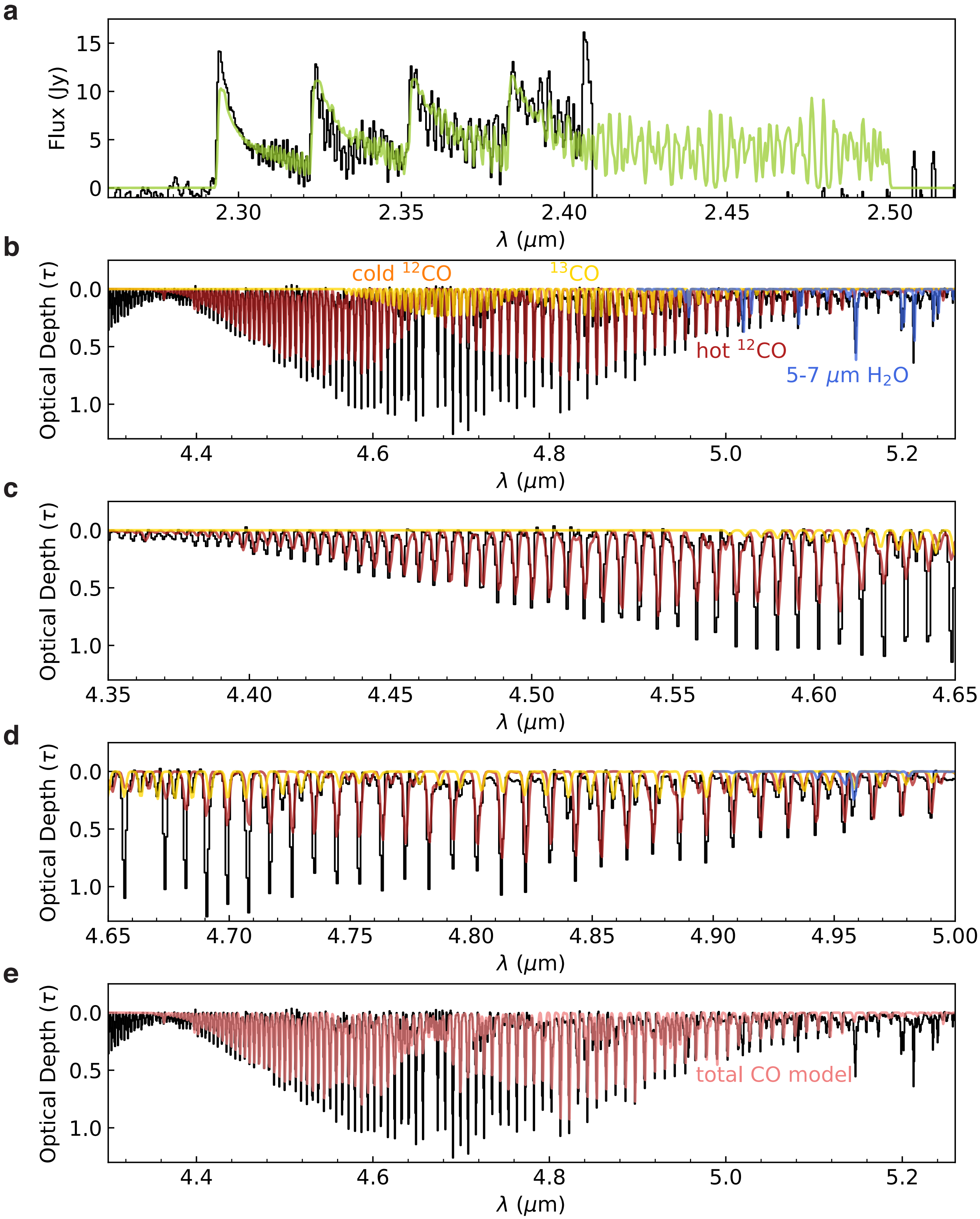

Extended Data Fig. 7 | Slab model fits for the CO vapour. a, The overtone v = 2-0, 3-1 and 4-2 bands appear in emission and trace hot, dense gas above the temperature inversion layer. **b**, The CO fundamental v = 1-0 band shows at least three absorption components, of which we fit two: hot ^{12}CO and warm ^{13}CO components that trace the inner edge of the thermostat region. The residuals of these fits indicate a missing cold ^{12}CO component, with a more complex geometry than is appropriate for our model. **c**,**d**, Zoom-in on individual lines, to show the quality of the fit. **e**, The sum of all three modelled CO components compared with the observational data. Residuals owing to a cold component with a different covering fraction are discussed in Methods and Supplementary Fig. 11.

Extended Data Table 1 | Results of infrared dust fitting

Name	Material	N_{solid} $[\times 10^{17}\ \mathrm{cm}^{-2}]$			
		M5(w)	M4(w)	M5(s)	M4(s)
Forsterite	Mg_2SiO_4	$1.3_{0.5}^{1.8}$	$1.2_{1.2}^{1.3}$	$2.0_{1.8}^{2.3}$	$1.4_{1.2}^{1.6}$
Enstatite	$MgSiO_3$	$3.7_{2.9}^{4.3}$	$4.8_{4.7}^{4.9}$	$4.1_{4.0}^{4.3}$	$4.4_{4.1}^{4.6}$
Silica	α-SiO_2	$1.4_{1.3}^{1.6}$	-	$2.7_{2.6}^{2.9}$	-
Interstellar	‘GCS3’	17_{16}^{18}	18_{17}^{19}	16_{14}^{16}	18_{17}^{19}
Blended ice	H_2O	40_{38}^{42}	43_{41}^{44}	39_{37}^{40}	41_{39}^{42}
Blended ice	CO_2	$3.1_{2.9}^{3.3}$	$3.2_{3.1}^{3.3}$	$2.8_{2.7}^{2.9}$	$3.0_{2.9}^{3.1}$
$N_{enstatite}/N_{forsterite}$		$2.8_{1.6}^{8.6}$	$4.0_{3.6}^{4.1}$	$2.05_{1.7}^{2.4}$	$3.1_{2.6}^{3.8}$
χ_r^2		7.28	8.13	6.71	14.37
AIC		17.29	16.14	16.72	22.37

The top rows list for each mineral the material, the reference for the laboratory data and the column density, N_{solid}, found from each of the four models we considered (see Methods). GCS3 refers to Galactic Center Silicates 3 (see Methods). The bottom rows list the ratio of enstatite to forsterite, along with the reduced chi-squared, χ_r^2, and AIC values for each of the four models. We report 3σ confidence intervals, not uncertainties.

Extended Data Table 2 | Results of infrared molecular gas fitting

Molecule	λ [μm]	T [K]	N [cm^{-2}]	ΔV [km s^{-1}]	R [au]
Absorption					
SiO	7.8-8.6	472^{478}_{468}	$4.62^{4.76}_{4.48}\times10^{18}$	$13.4^{13.6}_{13.2}$	1.07-1.24
C_2H_2	13.7	715^{1092}_{490}	$5.93^{12.10}_{3.61}\times10^{15}$	$45.9^{80.4}_{14.4}$	0.09-0.10
HCN	14	517^{556}_{484}	$2.73^{2.98}_{2.50}\times10^{16}$	$58.1^{84.7}_{21.8}$	0.06-0.07
H_2O	2.7-3.0	401^{402}_{400}	$4.20^{4.23}_{4.17}\times10^{19}$	$24.4^{24.5}_{24.3}$	0.32-0.37
H_2O	5-7	443^{444}_{442}	$2.64^{2.66}_{2.62}\times10^{19}$	$20.6^{20.7}_{20.6}$	0.46-0.52
H_2O	15-17	524^{538}_{509}	$2.71^{3.27}_{2.31}\times10^{18}$	$4.53^{4.96}_{4.10}$	9.4-10.7
CO_2	4.2-4.4	351^{353}_{348}	$1.81^{1.84}_{1.78}\times10^{17}$	$23.6^{24.1}_{23.2}$	0.35-0.39
CO_2	14.7-15.5	124^{135}_{114}	$1.23^{2.36}_{0.66}\times10^{19}$	$3.51^{3.71}_{3.34}$	15.7-17.9
^{12}CO	4.4-5.1	1181^{1188}_{1174}	$7.39^{7.51}_{7.30}\times10^{18}$	$37.7^{38.1}_{37.4}$	0.14-0.15
^{13}CO	4.4-5.1	646^{665}_{627}	$9.14^{9.33}_{8.96}\times10^{17}$	$36.1^{38.9}_{33.7}$	0.15-0.17
Emission					
^{12}CO	2.29-2.4	3754^{3800}_{3710}	$2.40^{2.45}_{2.34}\times10^{21}$	fixed 37.7	$0.543^{0.551}_{0.535}$

For each molecular band, we report its observed wavelength range and modelled temperature, column density, linewidth and range of disk radii in astronomical units (AU) implied by that linewidth, assuming disk Keplerian motion and no turbulence, for two limiting cases of the disk atmosphere and disk midplane, respectively. The CO emission band radius was determined differently from the absorption radii (see Methods). We report 1σ confidence intervals, not uncertainties.